PHYSICAL REVIEW B **108**, 064407 (2023)

Paramagnetic spin transport in a one-dimensional model

Weidi Wang, Lei Qiu, and Ka Shen*
The Center for Advanced Quantum Studies and Department of Physics, Beijing Normal University, Beijing 100875, China

(Received 16 May 2023; revised 12 July 2023; accepted 27 July 2023; published 8 August 2023)

We theoretically study paramagnetic spin transport based on atomistic simulations of spin dynamics in a one-dimensional model in the presence of a magnetic field along the transport direction. As the magnetic field increases, the spin diffusion length with an antiferromagnetic coupling between neighboring spins presents an interesting nonmonotonic behavior, which is attributed to the competition between the field-driven ordering in the low-field region and the reduction in the paramagnon lifetime in the high-field region. The local increase in magnon temperature in the ordered configuration, although of the same order as or even larger than the background temperature, is found to play a minor role in the spin diffusion length, suggesting that the temperature dependence of the paramagnon transport is mainly dominated by the magnon-phonon scattering.

DOI: 10.1103/PhysRevB.108.064407

I. INTRODUCTION

Spin transport, one of the central focuses of spintronics, has been extensively studied in both nonmagnetic and magnetic materials over the past few decades [1–3]. While the flow of the spin angular momentum in metallic systems is mainly carried by the conducting electrons, spin transport in magnetic insulators relies on the propagation of magnons [4,5]. Magnon-based spin transport has several advantages, such as the absence of Joule heating, tunable frequencies, and long propagation distances [6]. Since strong interactions between localized spins could benefit the formation and propagation of magnons, most studies on magnon spin transport have been performed in ferromagnets [7], ferrimagnets [8], and, recently, antiferromagnets [9–12], where the exchange interactions are sufficiently strong to order the spins.

Interestingly, it was demonstrated recently that paramagnetic insulators [13], in which the spin interactions are too weak to establish a magnetic order, could also host various spin-related phenomena, such as spin pumping [14], spin Hall magnetoresistance [15–18], and the spin Seebeck effect [19–24], implying the existence and good transport properties of so-called paramagnons [19], i.e., the local excitation of the short-distance magnetic order. As expected, the spin diffusion length of paramagnons was found to be rather short, namely, less than 1 nm in gadolinium gallium garnet (GGG) according to longitudinal spin Seebeck measurements at room temperature [25]. However, a recent nonlocal measurement showed that the spin current in GGG can transport over several microns at low temperature [4], comparable to or even longer than that in typical magnetic ordered systems. Such a long-distance paramagnetic spin transport was suggested to result from the extremely high group velocity of the backward volume magnetostatic waves. The irrelevance of such modes in the longitudinal spin Seebeck geometry may explain the much shorter spin diffusion length in Ref. [25].

In contrast to the complicated scenario of nonlocal geometry, the spin angular momenta in the longitudinal spin Seebeck geometry flow along the normal direction of the interface with nonequilibrium spin density uniformly distributed within the lateral plane, which in some sense can be regarded as a one-dimensional transport and can reflect the bulk transport properties of paramagnons. On the other hand, it was also suggested that the thermal conductivity mismatch at the interface might also play a crucial role in the paramagnetic spin Seebeck signal, which could hinder the identification of the intrinsic transport properties of paramagnons [19]. In the present work, we revisit the problem of paramagnon transport by theoretically simulating the spin dynamics in a weakly exchange coupled antiferromagnetic (AFM) spin chain, from which we surprisingly find a nonmonotonic magnetic field dependence of the paramagnon spin diffusion, rather than a monotonic feature as in the ferromagnetic (FM) case. The monotonic behavior is explained as the competition between the field-driven ordering and the enhanced magnetic damping due to the field-induced magnon gap. Moreover, we analyze the properties of the paramagnon lifetime using different mechanisms and recognize the dominant role of magnon-phonon scattering in the temperature dependence of paramagnon diffusion for the parameter region under study.

II. MODEL AND METHOD

Our minimal model is illustrated in Fig. 1(a), a one-dimensional spin chain consisting of N sites with a spacing of d between the neighbors. The Hamiltonian can be written as

$$H = H_0 + H_{\text{ex}} + H_{\text{DDI}}, \tag{1}$$

---

*kashen@bnu.edu.cn

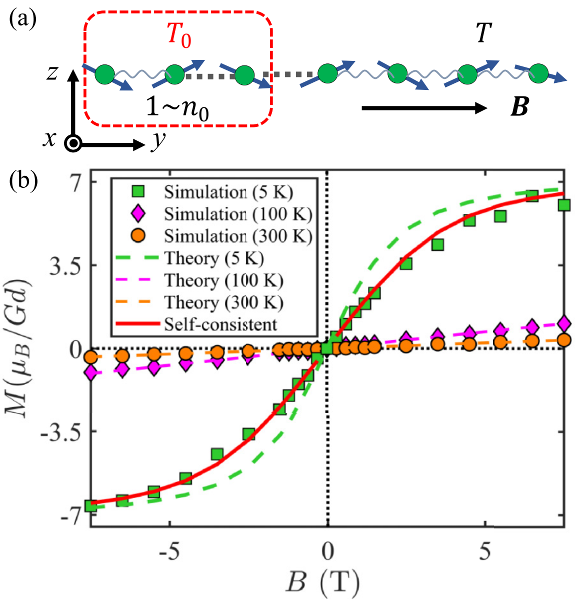

FIG. 1. (a) Schematics of a one-dimensional spin chain magnetized by a magnetic field along the chain. (b) Simulated magnetization as a function of the magnetic field at 5 K (green squares), 100 K (purple diamonds), and 300 K (orange circles). The dashed curves are the corresponding theoretical values from the Brillouin function. The red solid curve is from a self-consistent calculation explained in Appendix A.

where the first term is the Zeeman energy due to the external magnetic field,

$$H_0 = -\sum_i \boldsymbol{m}_i \cdot \boldsymbol{B}, \tag{2}$$

with the magnitude of the magnetic moment at each site being $m_i = g\mu_B\sqrt{S_i(S_i+1)}$. The magnetic field is applied along the chain in the y direction. The second term corresponds to the isotropic exchange interaction between all nearest neighbors,

$$H_{\text{ex}} = \frac{J}{(g\mu_B)^2}\sum_{\langle i,j\rangle} \boldsymbol{m}_i \cdot \boldsymbol{m}_j. \tag{3}$$

The third term in Eq. (1) refers to the classical dipole-dipole interaction (DDI) expressed as

$$H_{\text{DDI}} = \frac{\mu_0}{8\pi}\sum_{i\neq j}\frac{|\boldsymbol{r}_{ij}|^2\boldsymbol{m}_i\cdot\boldsymbol{m}_j - 3(\boldsymbol{m}_i\cdot\boldsymbol{r}_{ij})(\boldsymbol{m}_j\cdot\boldsymbol{r}_{ij})}{|\boldsymbol{r}_{ij}|^5}, \tag{4}$$

where $\boldsymbol{r}_{ij}$ represents the relative position between the ith and jth spins.

The spatiotemporal dynamics of the spin chain can be described by the Landau-Lifshitz-Gilbert equation

$$(1+\alpha^2)\frac{d\boldsymbol{m}_i}{dt} = -\gamma\boldsymbol{m}_i \times \boldsymbol{B}_i^{\text{eff}} - \frac{\alpha\gamma}{m_i}\boldsymbol{m}_i \times \left(\boldsymbol{m}_i \times \boldsymbol{B}_i^{\text{eff}}\right), \tag{5}$$

where α and $\gamma = g\mu_B/\hbar$ stand for the Gilbert damping and gyromagnetic ratio, respectively. The effective field $\boldsymbol{B}_i^{\text{eff}}$ is given by

$$\boldsymbol{B}_i^{\text{eff}} = \boldsymbol{B}_i^{\text{T}} - \frac{\partial H}{\partial \boldsymbol{m}_i}. \tag{6}$$

Here, the thermal fluctuation is introduced as a stochastic field $\boldsymbol{B}_i^{\text{T}}$, which follows a normal distribution satisfying [26–28]

$$\left\langle B_i^{\text{T}}(t)\right\rangle = 0, \tag{7}$$

$$\left\langle B_i^{\text{T}}(t)B_j^{\text{T}}(t')\right\rangle = \frac{2k_{\text{B}}T\alpha}{\gamma m_i}\delta_{ij}\delta(t-t'). \tag{8}$$

It is noteworthy that, without capturing explicitly the frequency and momentum dependences, the magnon-phonon interactions are taken into account via two aspects in this formalism. First, as an insulator, the magnon-phonon interactions are the main origin of Gilbert damping [29], physically corresponding to the magnon dissipation via phonon emission processes. Second, the phonon-induced thermal fluctuation field acting on the magnetization is introduced as a stochastic field [30], which triggers fluctuation to magnetization, i.e., the excitation of magnons.

For the numerical calculation below, we adopt the material parameters of GGG [31–33] with $g = 2$, $S = 7/2$, and the AFM exchange constant $J = 1.477 \times 10^{-24}$ J (corresponding to a temperature scale of 0.107 K) between the neighboring magnetic Gd atoms with a distance $d \approx 3.781$ Å. By numerically solving Eq. (5) in the time domain based on the integration method in Ref. [34], we extract the thermal properties of the spin dynamics at finite temperatures. The time step of $\Delta t = 1$ fs is used to converge the results with a damping constant $\alpha = 0.001$. The simulated equilibrium magnetization averaging over all sites for a long time is plotted as a function of the applied magnetic field at different temperatures in Fig. 1(b), which shows nice agreement with the theoretical result predicted by the Brillouin function (corresponding to the dashed curve of the same color), especially for those at 100 and 300 K. The deviation of the simulated curve from the theoretical one at 5 K reflects the influence of the finite effective field from the antiferromagnetic exchange, which can be corrected by a self-consistent calculation explained in Appendix A [see the red solid curve in Fig. 1(b)]. As the large magnetic field orders the magnetic moments at low temperature, spin transport in the form of paramagnons becomes possible.

To characterize the spin transport properties of paramagnons, we introduce a nonequilibrium distribution locally in the simulation by constructing a temperature step with n_0 sites on the left end of the chain of a much higher local temperature T_0. The higher-temperature sites then have a large local density of thermal paramagnons, which can diffuse to the other sites of the chain with a lower temperature T due to the spin interactions. Starting from an arbitrary spin configuration, the spin chain in our simulation reaches steady state within 10 ns of initialization, after which we analyze the characteristics of the transport properties from the spatial distribution of the paramagnons. Specifically, we collect all data in a period of 2 ns after the initialization and calculate the equal-time and space correlation function [28]

$$\boldsymbol{\mathcal{S}}_i = \langle \boldsymbol{m}_i \times \dot{\boldsymbol{m}}_i \rangle, \tag{9}$$

which is proportional to the measurable spin pumping efficiency at the interface between the magnetic system and a heavy metal [35,36]. Here, $\langle\cdot\rangle$ corresponds to the time average. The nonequilibrium paramagnon density is then given by

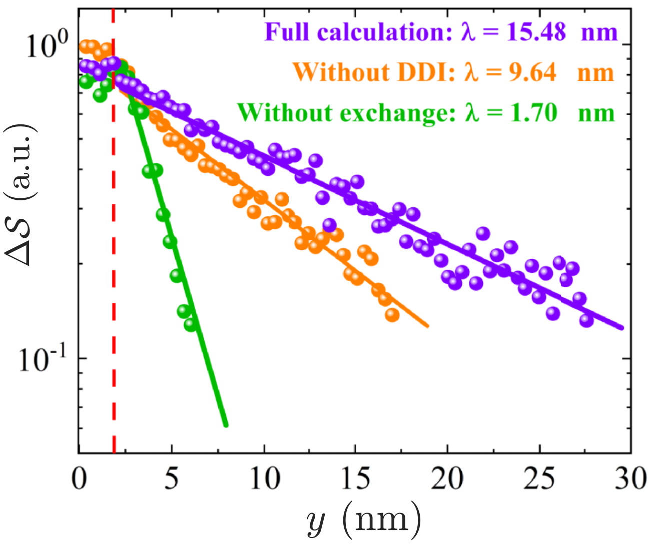

FIG. 2. The spatial distribution of the nonequilibrium paramagnon density from the calculation with different types of interactions. The dots are the calculated data, and the solid lines are the fitting curves. The red dashed line shows the location of the temperature step in the simulation. In this calculation, we take $B = 3.5$ T and $T = 5$ K.

$\Delta\boldsymbol{\mathcal{S}}_i = \boldsymbol{\mathcal{S}}_i - \boldsymbol{\mathcal{S}}^{\rm e}$, where the equilibrium density $\boldsymbol{\mathcal{S}}^e$ is calculated from the same simulation but without local heating. In the configuration shown in Fig. 1(a), we have $\mathcal{S}_i^x \approx \mathcal{S}_i^z \ll \mathcal{S}_i^y$, indicating that the angular momentum of the paramagnons is along the direction of the magnetic field. For a diffusive transport, the nonequilibrium quantities follow an exponential decay, i.e.,

$$\Delta\mathcal{S}_i^y \propto e^{-y/\lambda}, \tag{10}$$

from which we extract the diffusion length λ. The details of data processing are shown in Appendix B.

III. DIFFUSION LENGTH OF PARAMAGNONS

In this section, we analyze the role of different interactions in the paramagnon transport. The length of the chain is set to $N = 200$, which, as shown below, is sufficiently long compared to the diffusion length. The results from explicit simulations with parameters $B = 3.5$ T, $T = 5$ K, and $T_0 = 500$ K are plotted in Fig. 2, where the spins in the diffusion region are well magnetized according to Fig. 1(b). Note that the value of T_0 is actually not crucial because, as we will show below, the diffusion properties are extracted from the spins in the diffusion region where the magnon effective temperature is only slightly higher than T. As can be seen, the spin diffusion length from a full calculation can reach as far as 15 nm, despite the fact that both DDI and the exchange interaction are rather weak compared to those of typical ferromagnetic magnetic materials. It is worth noting that although this diffusion length does not reflect the exact spin diffusion in GGG, where the magnetic atoms do not align in a straight chain in real space, it provides a reasonable estimation of the scale and also allows qualitative analysis later of the dependences on parameters such as the magnetic field and the temperature. Figure 2 also shows that the diffusion length from the calculation without exchange interaction or DDI becomes considerably shorter than that from the full calculation, indicating their relevance in paramagnon transport.

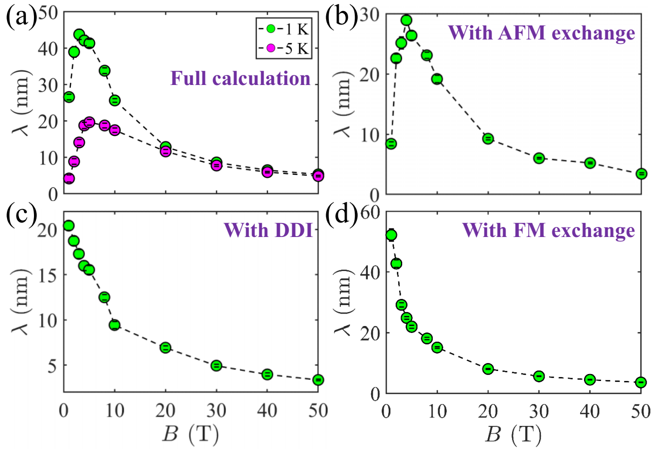

FIG. 3. Paramagnon diffusion length as a function of the magnetic field from calculations (a) with both DDI and AFM exchange interaction, (b) with AFM exchange interaction but without DDI, (c) with DDI (amplified five times for numerical reasons) but without exchange interaction, and (d) without DDI but with FM exchange interaction. The error bars represent the 95% confidence level.

A. Magnetic field dependence on the paramagnon diffusion

Next, we study explicitly the dependences of the paramagnon diffusion length on magnetic field. The results from the full calculation at different temperatures are plotted in Fig. 3(a), where the diffusion length first increases and then decreases with increasing magnetic field, displaying an interesting nonmonotonic behavior with a maximal diffusion length achieved around 3 and 5 T for 1 and 5 K, respectively. One might notice that a similar nonmonotonic behavior was reported in the nonlocal measurement of paramagnon transport in GGG [4], which, however, we would like to point out is not sufficient to conclude the same dependence of the paramagnon diffusion length because the nonlocal signal relies on not only the spatial decay but also the thermally injected density of the paramagnons. The latter might also contribute to the observed magnetic field dependence.

In order to disclose the origin of the nonmonotonic behavior in the field dependence of the paramagnon diffusion length, we simulate the cases with the AFM exchange interaction and DDI considered separately and plot the results in Figs. 3(b) and 3(c). While the nonmonotonic feature still survives in the calculation without DDI, the diffusion length with DDI (the magnitude is amplified five times for a reasonable fitting in the low-field region) but without AFM exchange interaction shows only a decrease with increasing magnetic field. As a comparison, we also perform a calculation in a ferromagnetic chain (changing the sign of the exchange parameter) with DDI excluded. As shown in Fig. 3(d), again, the nonmonotonic feature is absent. Thus, we conclude that the AFM exchange interaction is the key for the nonmonotonic magnetic field dependence of the paramagnon diffusion length

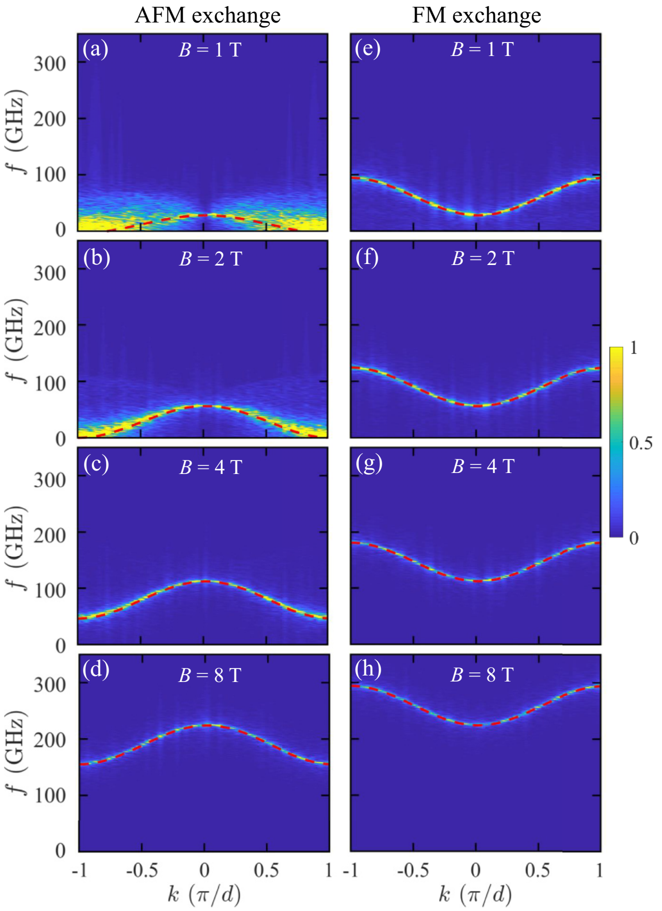

FIG. 4. The dispersion relations of the AFM and FM chains without DDI under a periodic boundary condition for different magnetic fields at $T = 1$ K. The dashed curves are analytical results from Eq. (11).

in Fig. 3(a). The reason might be related to the fact that the AFM exchange field prefers antiparallel alignment of the adjacent spins, while both the FM exchange interaction and the dipole field in the present configuration pull all spins in the same direction.

1. *Low magnetic field behavior*

To further explore the underlying physics behind the anomalous low-field increase of the paramagnon diffusion in an AFM chain, we calculate the dispersion relations of the paramagnon in AFM and FM chains by Fourier transforming the spatiotemporal evolution of the transverse magnetization components under a periodic boundary condition. The results at $T = 1$ K are plotted in Fig. 4 with different values of the magnetic field. Assuming that the magnetic field is large enough to overcome the exchange one (~0.63 T at zero temperature) and establish a stable magnetic order, the dispersion relation is given by

$$\omega_k = \gamma[B - 2B_{\rm ex}(1 - \cos kd)], \tag{11}$$

where the effective field from the exchange interaction is defined as $B_{\rm ex}(T) = 2Jm_i^y(T)/(g\mu_B)^2$, with $m_i^y(T)$ being the long-time average value of the longitudinal component along the magnetic field with thermal magnon excitation taken into account [37]. The dispersion relations from Eq. (11) are plotted as red dashed curves in Fig. 4, which show nice agreement with the simulated ones. As seen in Fig. 4(a), for the AFM chain at 1 T, the dispersion curve has a negative frequency region with very large broadening, indicating that the magnetic moments are not well ordered. Because the external magnetic field exerted on magnetic sites is compensated by the exchange interaction according to Eq. (11), the net magnetic field $B_{\rm net} = |B - 2B_{\rm ex}| \sim 0.26$ T is smaller than the random field from the thermal fluctuation (1.46 T at $T = 1$ K). For the FM chain, the negative value of $B_{\rm ex}$ leads to a sufficient $B_{\rm net}$ for a stable magnetic order at the same value of external field [see Fig. 4(e)]. As the negative frequency is pushed away by a magnetic field around 2 T, the broadening of the dispersion curve in Fig. 4(b), however, remains very large. This reflects a very short paramagnon lifetime and can be understood to be a consequence of the frequent scattering processes among the large number of thermal paramagnons, as well as their interactions with phonons.

As the magnetic field increases further, the thermal generation of paramagnons is suppressed by the enlarged magnon gap, which, on the one hand, leads to a decrease in the magnon-magnon and/or magnon-phonon scatterings and shrinks the linewidth and, on the other hand, modifies the paramagnon dispersion with a slightly larger group velocity, as shown in Fig. 4(c). For a qualitative analysis of the calculated paramagnon diffusion length, we employ a simple expression averaged over all states:

$$\lambda_{\rm eff} = \frac{\sum_k \tau_k v_k N(\omega_k)}{\sum_k N(\omega_k)}, \tag{12}$$

where τ_k is the paramagnon lifetime, v_k is the group velocity, and $N(\omega_k)$ is the Bose-Einstein distribution function. Equation (12) thus suggests that the increase in the diffusion length in Fig. 3(b) below 4 T should result from the combination of the extended lifetime and the enlarged group velocity.

2. *High magnetic field behavior*

In the high magnetic field region, the shape of the dispersion curve and hence the group velocity become insensitive to the further increase of the magnetic field, which suggests that the decrease of diffusion length in Fig. 3(b) must originate from the magnetic dependence of the paramagnon lifetime. To extract the paramagnon lifetime directly, we fit the Fourier spectrum at any given wave vector by the Lorentz function

$$C(f) = \frac{A}{(f - \omega_k)^2 + 1/(2\pi\tau_k)^2}. \tag{13}$$

An example of the fitting for the data with $B = 4$ T and $k = 0.1(\pi/d)$ from Fig. 4(c) is shown in Fig. 5(a). The obtained paramagnon frequencies and the corresponding lifetimes with different values of wave vectors and magnetic fields are summarized in Fig. 5(b). In general, as the magnetic field increases, the frequency of the paramagnon shifts to the higher-frequency region, and in the meantime, the lifetime becomes shorter and is distributed over a smaller range. The solid curve illustrates the phenomenological lifetimes,

$$\tau_k^0 = 1/(\alpha\omega_k), \tag{14}$$

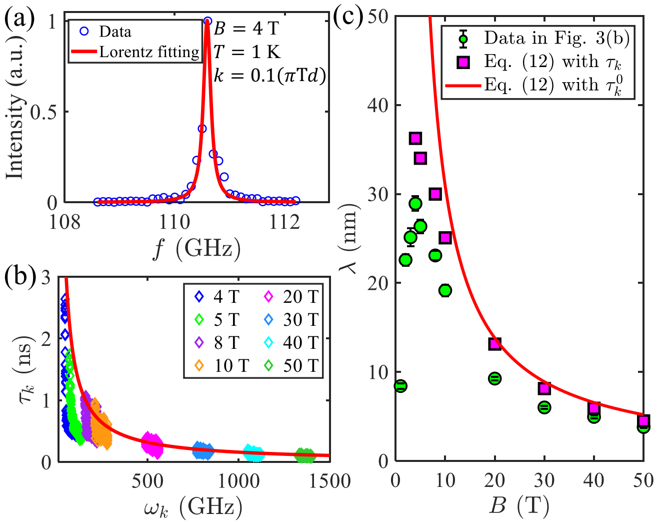

FIG. 5. (a) Lorentz fitting of the Fourier spectrum with a given wave vector $k = 0.1(\pi/d)$ at $B = 4$ T and $T = 1$ K. (b) The relation between the paramagnon lifetime τ_k and the resonant frequency ω_k from Lorentz fitting (diamonds) with different values of the magnetic field at $T = 1$ K and the phenomenological relation $\tau_k^0 = 1/(\alpha\omega_k)$ (red curve). (c) Comparison of the simulated diffusion length in Fig. 3(b) and the theoretical values calculated from Eq. (12) with τ_k and τ_k^0.

which shows excellent agreement with the trend of the simulated lifetimes. This indicates that the magnetic damping related to phonon emission dominates the decay of the angular momentum during diffusion and the magnon-magnon scattering and magnon-phonon scattering due to the thermal fluctuation field are irrelevant in the high magnetic field region. That is because of the very low densities of the magnons and phonons at $T = 1$ K.

By substituting the above paramagnon lifetimes τ_k and τ_k^0 separately in Eq. (12), we calculate the effective paramagnon diffusion lengths and plot them as a function of the magnetic field in Fig. 5(c), which agrees well with those from direct simulations [the green dots, which are the same as those in Fig. 3(b)] in the high magnetic field region.

B. Magnon-magnon scattering vs magnon-phonon scattering

After a close comparison with the lifetimes in Fig. 5(b), one may notice that the lifetime obtained from the Fourier spectrum τ_k is always smaller than the phenomenological one τ_k^0, reflecting the influence of the magnon-magnon scattering and/or magnon-phonon scattering induced by thermal fluctuation. In this section, we analyze the relative contribution of these two mechanisms based on their different dependences on (local) magnon effective temperature and phonon temperature [29,38].

In our transport simulation above for Fig. 3, the local temperature on the left side of the spin chain is set to be much higher than the transport region, which forms a nonequilibrium magnon accumulation around the boundary of the heat source. To quantitatively evaluate the local nonequilibrium intensity of the paramagnons in the transport condition, we plot the spatial distribution of the temporally averaged magnetization $\langle m_i^y\rangle$ of the AFM chain, instead of $\Delta\mathcal{S}$ for Fig. 2, as the green squares in Fig. 6(a) for $B = 4$ T and $T = 1$ K, which indeed shows a remarkable reduction from the equilibrium value (yellow diamonds without a heat source) as far as tens nanometers from the heating area. To describe the density of nonequilibrium magnons due to the deviation of the magnetization from its equilibrium value, we use the language of the local magnon effective temperature, which is estimated by reading the effective temperature at the magnetization $\langle m_i^y\rangle$ in the temperature dependence of the equilibrium magnetization [see Fig. 1(b)], plotted in the inset in Fig. 6(b). One can see that the local increase in the paramagnon temperature near the heating area ($\Delta T_i^{\rm m} \sim 10$ K) can even be one order of

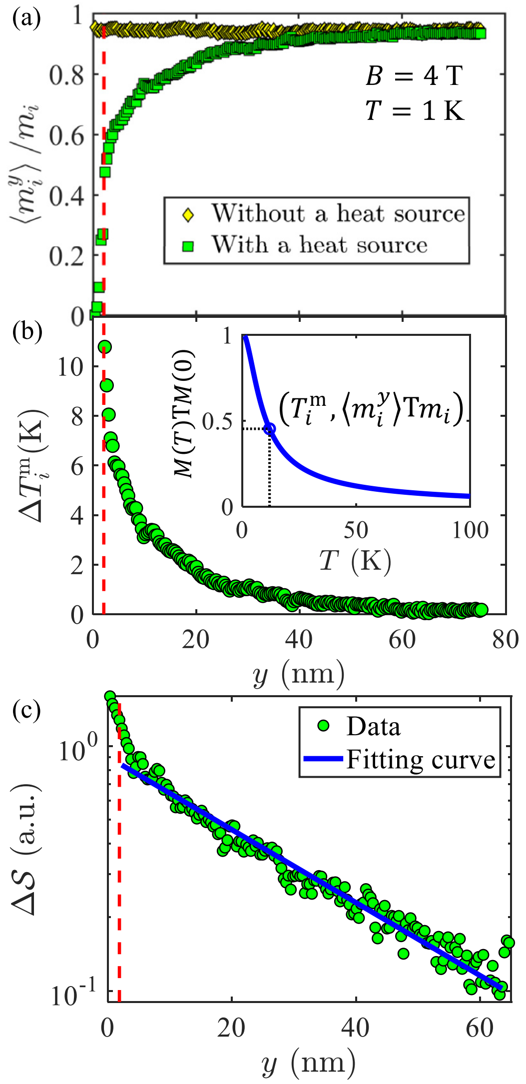

FIG. 6. (a) Local magnetization with (green squares) and without (yellow diamonds) local heating at 1 K for the AFM chain (with DDI excluded) under a magnetic field of 4 T. (b) Spatial distribution of the rise of the effective paramagnon temperature. The red dashed curve indicates the boundary of the local heating (with $T_0 = 500$ K). The inset in (b) shows the method to evaluate the effective paramagnon temperature from the temperature dependence of the equilibrium magnetization. (c) The spatial distribution of the nonequilibrium paramagnon density of the AFM chain.

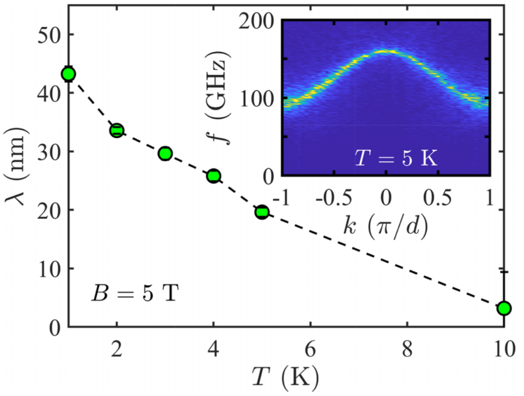

FIG. 7. Phonon temperature dependence of the paramagnon diffusion length from the full calculation with the magnetic field at 5 T, for which we vary T with a constant value of T_0. The error bars represent the 95% confidence level. The inset shows the paramagnon spectrum simulated at 5 K.

magnitude higher than the local phonon temperature ($T = 1$ K), indicating a large value of the nonequilibrium magnon density. This might also imply that the magnon-magnon scattering in the transport case is enhanced compared to the equilibrium condition at $T = 1$ K. However, the spatial distribution of the nonequilibrium quantity ΔS plotted in Fig. 6(c) still presents a very nice single exponential decay in the entire transport region, except the position very close to the heat source. This means that the increase of the local magnon temperature is actually not crucial for the paramagnon lifetime and paramagnon diffusion length for the temperature and magnetic field region adopted in this calculation. Therefore, we conclude that the magnon-phonon scattering dominates the scattering mechanism for the low-temperature transport in the present case.

The influences of the magnon-phonon scattering can actually be seen in Fig. 3(a), where the paramagnon diffusion length from the full calculation at 5 K is found to be much shorter than that at 1 K in the relatively low magnetic field region. In Fig. 7, we explicitly show a monotonic decrease of the paramagnon diffusion length with increasing temperature under a magnetic field at $B = 5$ T. As the shape of the paramagnon spectrum plotted in the inset remains almost the same as those in Figs. 4(c) and 4(d) at 1 K, the broadening of the spectrum becomes much larger, corresponding to a smaller paramagnon lifetime, as expected from the stronger magnon-phonon scattering.

IV. SUMMARY

In summary, based on atomistic simulations, we studied paramagnetic spin transport in a one-dimensional spin chain with a weak antiferromagnetic exchange interaction between the spins, where we predicted a nonmonotonic magnetic field dependence of the paramagnon diffusion length. We found that such a nonmonotonic behavior originates from the antiferromagnetic exchange interaction, which gives rise to an interplay between the field-induced magnetic order in the low-field region and the larger dissipation rate proportional to the frequency in the high-field region. Moreover, the magnon-magnon scattering was found to play only a marginal role in the paramagnon diffusion, while the magnon-phonon scattering dominates the decrease of the diffusion length as the temperature increases. Although our simulations were performed mainly at low temperatures, the prediction of the nonmonotonic magnetic field dependent paramagnon diffusion length may be valid at higher temperatures as well, where the large thermal fluctuation, however, requires a rather long simulation time to achieve convergence.

It is also worth pointing out that the quantum effects could become relevant to the low-temperature spin dynamics when the thermal fluctuation is too weak to excite high-frequency magnons, resulting in the suppression of the interactions between magnons. As such effects can be nicely captured via a quantum thermostat even without self-consistent treatment of the temperature-dependent magnon spectrum and population [39,40], they will not change the predicted nonmonotonic behavior. The reason is that thanks to the weak DDI and exchange interaction, the high-frequency magnons exist only in the high magnetic field region, where the magnon-magnon interactions have only negligible influence on the magnon lifetime according to Fig. 5(b).

ACKNOWLEDGMENTS

This work was supported by the National Natural Science Foundation of China (Grant No. 11974047) and the Fundamental Research Funds for the Central Universities.

APPENDIX A: SELF-CONSISTENT CALCULATION OF MAGNETIZATION

According to the quantum statistical theory, the average magnetization of an individual spin under a magnetic field B_0 can be described by the Brillouin function $B_s(x)$ as

$$\langle m\rangle = Sg\mu_B B_s(x), \tag{A1}$$

with $x = Sg\mu_B B_0/k_B T$. In our case, the exchange and dipole-dipole interactions also contribute to the effective magnetic field, so we need to replace B_0 in Eq. (A1) by

$$B_{\mathrm{eff}} = B + 2\frac{\langle m\rangle}{m_i}(B_{\mathrm{ex}} + B_{\mathrm{DDI}}), \tag{A2}$$

where B_{ex} and B_{DDI} stand for the exchange and dipolar fields given by Eq. (6). The average magnetization $\langle m\rangle$ can then be determined self-consistently from Eqs. (A1) and (A2).

The quantitative comparison between the quantum expression (A1) and our classical simulation in Fig. 1 relies on the condition of the maximal magnon energy, $\hbar\omega_k^{\max} \ll k_{\mathrm{B}}T$, which is satisfied perfectly at 100 and 300 K. For $T = 5$ K, we have $\omega_k^{\max} \simeq 230$ GHz at 8 T, leading to $\hbar\omega_k^{\max}/k_{\mathrm{B}}T \sim 2$, which is still in the acceptable region for the approximation of the classical thermostat described by Eqs. (7) and (8) (see also Ref. [38]). From a close comparison to the Brillouin function in Fig. 1, we can see the simulated results at 5 K are systematically smaller, especially in the high-field region (corresponding to a larger magnon frequency), which

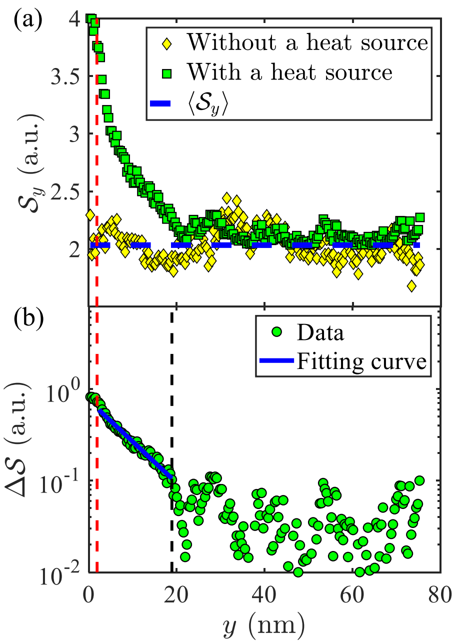

FIG. 8. The data processing for a AFM chain. (a) The variation of $\mathcal{S}_y$ with position y at $T = 5$ K. The red dashed line shows the location of the temperature step. (b) The black dashed line indicates the horizontal coordinate of y_1, and the solid blue line is the fitting curve.

may reflect the relevance of the quantum effects discussed in Sec. IV.

APPENDIX B: THE DETAILS OF DATA PROCESSING DURING DATA FITTING

Because all the data processing during fitting is the same, we take the AFM chain as an example to illustrate it. The location of the temperature step can be expressed as $y_0 = n_0 d = 1.89$ nm. By simulating the case of spin transport with and without a heat source, we calculate the $\mathcal{S}_y$ of each spin and draw it as a function of position y [Fig. 8(a)].

To characterize the spin transport signal caused by a heat source, we need to subtract the data without a heat source from the data with a heat source. So we can define $\Delta\mathcal{S} = \mathcal{S}_y - \langle \mathcal{S}_y \rangle$, where $\langle \mathcal{S}_y \rangle$ is the average of $\mathcal{S}_y$ among all spins for the case without a heat source. When $\Delta\mathcal{S}$ is very small (<0.1), we can consider the heat source to have no influence on the spin transport. The point $y_1 = 18.90$ nm is the first one that meets this condition, which is shown by the black dashed line in Fig. 8(b). In the region $y_0 < y \leqslant y_1$, $\Delta\mathcal{S}$ describes the diffusion of spin currents, and we fit the data [blue line in Fig. 8(b)], which gives the spin diffusion length $\lambda = 9.64 \pm 0.57$ nm.

---

[1] Y. Tserkovnyak, A. Brataas, and G. E. W. Bauer, Enhanced Gilbert Damping in Thin Ferromagnetic Films, Phys. Rev. Lett. **88**, 117601 (2002).

[2] Y. Tserkovnyak, A. Brataas, G. E. W. Bauer, and B. I. Halperin, Nonlocal magnetization dynamics in ferromagnetic heterostructures, Rev. Mod. Phys. **77**, 1375 (2005).

[3] I. Žutić, J. Fabian, and S. Das Sarma, Spintronics: Fundamentals and applications, Rev. Mod. Phys. **76**, 323 (2004).

[4] K. Oyanagi, S. Takahashi, L. J. Cornelissen, J. Shan, S. Daimon, T. Kikkawa, G. E. Bauer, B. J. van Wees, and E. Saitoh, Spin transport in insulators without exchange stiffness, Nat. Commun. **10**, 4740 (2019).

[5] Y. Kajiwara, K. Harii, S. Takahashi, J. Ohe, K. Uchida, M. Mizuguchi, H. Umezawa, H. Kawai, K. Ando, K. Takanashi, S. Maekawa, and E. Saitoh, Transmission of electrical signals by spin-wave interconversion in a magnetic insulator, Nature (London) **464**, 262 (2010).

[6] A. V. Chumak, V. I. Vasyuchka, A. A. Serga, and B. Hillebrands, Magnon spintronics, Nat. Phys. **11**, 453 (2015).

[7] J. König, M. C. Bønsager, and A. H. MacDonald, Dissipationless Spin Transport in Thin Film Ferromagnets, Phys. Rev. Lett. **87**, 187202 (2001).

[8] L. Cornelissen, J. Liu, R. Duine, J. B. Youssef, and B. Van Wees, Long-distance transport of magnon spin information in a magnetic insulator at room temperature, Nat. Phys. **11**, 1022 (2015).

[9] W. Xing, L. Qiu, X. Wang, Y. Yao, Y. Ma, R. Cai, S. Jia, X. C. Xie, and W. Han, Magnon Transport in Quasi-Two-Dimensional van der Waals Antiferromagnets, Phys. Rev. X **9**, 011026 (2019).

[10] R. E. Troncoso, S. A. Bender, A. Brataas, and R. A. Duine, Spin transport in thick insulating antiferromagnetic films, Phys. Rev. B **101**, 054404 (2020).

[11] Y. Cheng and S. Zhang, Spin transport in noncollinear antiferromagnetic metals, Phys. Rev. B **102**, 134403 (2020).

[12] Y. Zhou, T. Guo, L. Qiao, Q. Wang, M. Zhu, J. Zhang, Q. Liu, M. Zhao, C. Wan, W. He, H. Bai, L. Han, L. Huang, R. Chen, Y. Zhao, X. Han, F. Pan, and C. Song, Piezoelectric strain-controlled magnon spin current transport in an antiferromagnet, Nano Lett. **22**, 4646 (2022).

[13] S. Okamoto, Spin injection and spin transport in paramagnetic insulators, Phys. Rev. B **93**, 064421 (2016).

[14] Y. Shiomi and E. Saitoh, Paramagnetic Spin Pumping, Phys. Rev. Lett. **113**, 266602 (2014).

[15] L. Liang, J. Shan, Q. H. Chen, J. M. Lu, G. R. Blake, T. T. M. Palstra, G. E. W. Bauer, B. J. van Wees, and J. T. Ye, Gate-controlled magnetoresistance of a paramagnetic-insulator|platinum interface, Phys. Rev. B **98**, 134402 (2018).

[16] R. Schlitz, T. Kosub, A. Thomas, S. Fabretti, K. Nielsch, D. Makarov, and S. T. B. Goennenwein, Evolution of the spin hall magnetoresistance in Cr_2O_3/Pt bilayers close to the Néel temperature, Appl. Phys. Lett. **112**, 132401 (2018).

[17] K. Oyanagi, J. M. Gomez-Perez, X.-P. Zhang, T. Kikkawa, Y. Chen, E. Sagasta, A. Chuvilin, L. E. Hueso, V. N. Golovach, F. S. Bergeret, F. Casanova, and E. Saitoh, Paramagnetic spin Hall magnetoresistance, Phys. Rev. B **104**, 134428 (2021).

[18] V. Eswara Phanindra, A. Das, J. J. L. van Rijn, S. Chen, B. J. van Wees, and T. Banerjee, Spin Hall magnetoresistance across

a paramagnetic Pt/NdGaO$_3$ interface, Appl. Phys. Lett. **123**, 022410 (2023).

[19] S. M. Wu, J. E. Pearson, and A. Bhattacharya, Paramagnetic Spin Seebeck Effect, Phys. Rev. Lett. **114**, 186602 (2015).

[20] D. Hong, C. Liu, J. E. Pearson, A. Hoffmann, D. D. Fong, and A. Bhattacharya, Spin Seebeck effect in insulating SrFeO$_{3-\delta}$ films, Appl. Phys. Lett. **114**, 242403 (2019).

[21] A. Aqeel, N. Vlietstra, J. A. Heuver, G. E. W. Bauer, B. Noheda, B. J. van Wees, and T. T. M. Palstra, Spin-Hall magnetoresistance and spin Seebeck effect in spin-spiral and paramagnetic phases of multiferroic CoCr$_2$O$_4$ films, Phys. Rev. B **92**, 224410 (2015).

[22] J. Li, Z. Shi, V. H. Ortiz, M. Aldosary, C. Chen, V. Aji, P. Wei, and J. Shi, Spin Seebeck Effect from Antiferromagnetic Magnons and Critical Spin Fluctuations in Epitaxial FeF$_2$ Films, Phys. Rev. Lett. **122**, 217204 (2019).

[23] N. Ito, T. Kikkawa, J. Barker, D. Hirobe, Y. Shiomi, and E. Saitoh, Spin Seebeck effect in the layered ferromagnetic insulators CrSiTe$_3$ and CrGeTe$_3$, Phys. Rev. B **100**, 060402(R) (2019).

[24] K. Oyanagi, S. Takahashi, T. Kikkawa, and E. Saitoh, Mechanism of paramagnetic spin Seebeck effect, Phys. Rev. B **107**, 014423 (2023).

[25] H. Wang, C. Du, P. C. Hammel, and F. Yang, Spin transport in antiferromagnetic insulators mediated by magnetic correlations, Phys. Rev. B **91**, 220410(R) (2015).

[26] J. Zhu, Thermal magnetic noise and spectra in spin valve heads, J. Appl. Phys. **91**, 7273 (2002).

[27] J. Xiao, A. Zangwill, and M. D. Stiles, Macrospin models of spin transfer dynamics, Phys. Rev. B **72**, 014446 (2005).

[28] J. Barker and G. E. W. Bauer, Thermal Spin Dynamics of Yttrium Iron Garnet, Phys. Rev. Lett. **117**, 217201 (2016).

[29] J. Xiao, G. E. W. Bauer, K.-C. Uchida, E. Saitoh, and S. Maekawa, Theory of magnon-driven spin Seebeck effect, Phys. Rev. B **81**, 214418 (2010).

[30] J. Fidler and T. Schrefl, Micromagnetic modelling - The current state of the art, J. Phys. D: Appl. Phys. **33**, R135 (2000).

[31] O. A. Petrenko and D. McK. Paul, Classical Heisenberg antiferromagnet on a garnet lattice: A Monte Carlo simulation, Phys. Rev. B **63**, 024409 (2000).

[32] T. Yavors'kii, M. Enjalran, and M. J. P. Gingras, Spin Hamiltonian, Competing Small Energy Scales, and Incommensurate Long-Range Order in the Highly Frustrated Gd$_3$Ga$_5$O$_{12}$ Garnet Antiferromagnet, Phys. Rev. Lett. **97**, 267203 (2006).

[33] J. A. Paddison, H. Jacobsen, O. A. Petrenko, M. T. Fernández-Díaz, P. P. Deen, and A. L. Goodwin, Hidden order in spin-liquid Gd$_3$Ga$_5$O$_{12}$, Science **350**, 179 (2015).

[34] C. Serpico, I. D. Mayergoyz, and G. Bertotti, Numerical technique for integration of the Landau-Lifshitz equation, J. Appl. Phys. **89**, 6991 (2001).

[35] S. M. Rezende, R. L. Rodríguez-Suárez, R. O. Cunha, A. R. Rodrigues, F. L. A. Machado, G. A. Fonseca Guerra, J. C. Lopez Ortiz, and A. Azevedo, Magnon spin-current theory for the longitudinal spin-Seebeck effect, Phys. Rev. B **89**, 014416 (2014).

[36] E. Saitoh, M. Ueda, H. Miyajima, and G. Tatara, Conversion of spin current into charge current at room temperature: Inverse spin-Hall effect, Appl. Phys. Lett. **88**, 182509 (2006).

[37] K. Shen, Finite temperature magnon spectra in yttrium iron garnet from a mean field approach in a tight-binding model, New J. Phys. **20**, 043025 (2018).

[38] U. Ritzmann, D. Hinzke, and U. Nowak, Propagation of thermally induced magnonic spin currents, Phys. Rev. B **89**, 024409 (2014).

[39] J. Barker and G. E. W. Bauer, Semiquantum thermodynamics of complex ferrimagnets, Phys. Rev. B **100**, 140401(R) (2019).

[40] C. H. Woo, H. Wen, A. A. Semenov, S. L. Dudarev, and P.-W. Ma, Quantum heat bath for spin-lattice dynamics, Phys. Rev. B **91**, 104306 (2015).